Analyst

PAPER

View Article Online
View Journal | View Issue

Check for updates

Cite this: *Analyst*, 2023, **148**, 919

A chiral sensing platform based on a multi-substituted ferrocene–cuprous ion complex for the discrimination of electroactive amino acid isomers

Tai Wen,[a] Junyao Li,[a] Wenrong Cai,[a] Baozhu Yang,[a] Yong Kong *[a] and Zheng-Zhi Yin *[b]

Received 18th November 2022,
Accepted 11th January 2023

DOI: 10.1039/d2an01887j

rsc.li/analyst

An electrochemical chiral sensing platform based on a multi-substituted ferrocene–cuprous ion (Cu^+) complex is constructed for the discrimination of electroactive amino acid (AA) isomers. Due to the opposite configurations of the AA isomers, the developed multi-substituted ferrocene–Cu^+ can preferably combine with a right-handed AA (D-AA) isomer to form the ternary complex of multi-substituted ferrocene–Cu^+-D-AA through π–π interactions, resulting in higher peak currents of D-AA. Therefore, the isomers of electroactive AA can be successfully discriminated. Among the tested electroactive AA isomers, the chiral sensing platform exhibits higher discrimination capability toward the isomers of tryptophan (Trp) than that of tyrosine (Tyr) and cysteine (Cys), which might be ascribed to the stronger π–π interactions between the benzene ring of the multi-substituted ferrocene and the indole ring of the Trp isomers.

Published on 11 2023. Downloaded on 11.5.2026 19:23:17.

Introduction

Chirality is ubiquitous in nature and plays a crucial role in a variety of fields such as catalysis, medicine and food science.[1,2] For example, amino acids (AAs) are one kind of biologically active chiral substance in living organisms, which are the molecular building blocks of proteins.[3–5] However, only left-handed AAs (L-AA) are involved in the synthesis of proteins while right-handed AAs (D-AA) do not participate in protein synthesis and may even cause undesirable side-effects.[6,7] Therefore, the discrimination of chiral molecules such as AA isomers and chiral drugs has attracted increasing attention in recent years. Among the reported methods for chiral discrimination, electrochemical methods are especially attractive since they can easily convert architectural variation into discernible changes in electrochemical signals such as potential, current, and impedance.[8–15] However, no matter which electrochemical method is used, it is necessary to build chiral sensing platforms with enough discrimination capability.[16]

Chiral selectors play a pivotal role in the construction of chiral sensing platforms, which are usually composed of organic ligands and metal ions.[17,18] For instance, Tang *et al.*[19] reported the synthesis of (*S*)-BINAP-metal complexes as a chiral selector for the enantioselective extraction of phenylglycine isomers, and the addition of tetrakis(acetonitrile)copper(I) hexafluorophosphate ($[(CH_3CN)_4Cu]PF_6$) not only provides cuprous ions (Cu^+) but can also enhance the extraction efficiency of the chiral selector toward phenylglycine isomers.

2*R*-1-[(*S*)-α-(Dimethylamino)-2-(diphenylphosphino)benzyl]-2-diphenylphosphino ferrocene (Taniaphos) is an important multi-substituted ferrocene, which has been widely used as a catalyst for asymmetric synthesis.[20,21] Similar to (*S*)-BINAP, Taniaphos also possesses benzene rings in its molecule (Fig. 1), and thus it might be a competent chiral ferrocene ligand used for chiral separation and discrimination. For example, Xiao *et al.*[22] reported that Taniaphos–Cu^+ can be employed as a chiral extractant to enantioseparate various

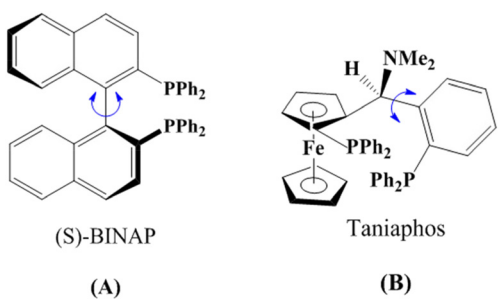

Fig. 1 Chemical structures of (*S*)-BINAP (A) and Taniaphos (B).

[a]*Jiangsu Key Laboratory of Advanced Catalytic Materials and Technology, School of Petrochemical Engineering, Changzhou University, Changzhou 213164, P. R. China. E-mail: yzkongyong@cczu.edu.cn*
[b]*College of Biological, Chemical Sciences and Engineering, Jiaxing University, Jiaxing 314001, P. R. China. E-mail: yinzhengzhi@zjxu.edu.cn*

Published on 11 2023. Downloaded on 11.5.2026 19:23:17.

amino acid enantiomers. However, as far as we are aware, Taniaphos and Taniaphos–metal complexes have never been utilized in the construction of chiral sensing platforms for the discrimination of AA isomers.

In this work, a complex of Taniaphos–Cu^+ was synthesized and used as the chiral selector for the construction of an electrochemical chiral sensing platform, which was utilized for the chiral discrimination of electroactive AA isomers including tryptophan (Trp), tyrosine (Tyr) and cysteine (Cys). The Taniaphos–Cu^+ complex-based chiral sensing platform could preferably combine with D-AA to form the ternary complex through π–π interactions, resulting in higher peak currents of D-AA. Compared with the Taniaphos chiral selector, higher discrimination capability, which was denoted by the peak current ratio of D-AA to L-AA ($I_{D\text{-}AA}/I_{L\text{-}AA}$), could be achieved with the Taniaphos–Cu^+ chiral selector. In addition, the developed chiral sensing platform displayed higher discrimination capability toward Trp isomers compared to Tyr and Cys isomers, which might be ascribed to the stronger π–π interactions between the benzene ring of Taniaphos and the indole ring of Trp.

Experimental

Reagents and apparatus

Taniaphos was purchased from Yien Chemical Technology Co., Ltd (Shanghai, China). $[(CH_3CN)_4Cu]PF_6$, 1,2-dichloroethane, L-/D-Trp and L-/D-Tyr were obtained from Aladdin Chemistry Co., Ltd (Shanghai, China). L-/D-Cys was obtained from Saen Chemical Technology Co., Ltd (Shanghai, China). Other reagents not mentioned were of analytical grade and were purchased from Sinopharm Chemical Reagent Co., Ltd (Shanghai, China). All aqueous solutions were prepared with ultrapure water (18.2 MΩ cm, Millipore).

Scanning electron microscopy (SEM) characterization of Taniaphos and the Taniaphos–Cu^+ complex was conducted with a Supra55 field-emission scanning electron microscope (Zeiss, Germany), and the Fourier transform infrared (FT-IR) spectra of $[(CH_3CN)_4Cu]PF_6$, Taniaphos and Taniaphos–Cu^+ were acquired with a Nicolet IS50 FT-IR spectrometer (Thermo Fisher Scientific, USA). The X-ray photoelectron spectroscopy (XPS) of the Taniaphos–Cu^+ complex was conducted by means of an Axis Ultra DLD X-ray photoelectron spectrometer (Shimadzu, Japan), and the water contact angles of stationary water droplets (2.0 μL) on different samples were measured with a DSA25 contact angle goniometer (Kruss GmbH, Germany). The electrochemical measurements, including cyclic voltammograms (CVs) and differential pulse voltammograms (DPVs), and electrochemical impedance spectroscopy (EIS), were carried out by using a CHI 660E electrochemical workstation (Shanghai Chenhua Instruments Co. Ltd, China).

Construction of the chiral sensing platform

First, the Taniaphos–Cu^+ complex was prepared by the previously reported method.[22] Briefly, 68.7 mg of Taniaphos and 37.7 mg of $[(CH_3CN)_4Cu]PF_6$, which was used as the metal precursor, were dissolved in 100 mL of 1,2-dichloroethane, and the resulting orange solution of the Taniaphos–Cu^+ complex was maintained at 4 °C for 12 h.

Next, 5.0 μL of the Taniaphos–Cu^+ complex solution (1.0 mM) was cast onto the surface of a glassy carbon electrode (GCE, 3 mm in diameter), which was polished with 0.05 μm alumina slurry before use. After the solvent was dried in ambient air, the chiral sensing platform (Taniaphos–Cu^+/GCE) was obtained. For control experiments, a Taniaphos-modified GCE (Taniaphos/GCE) and a $[(CH_3CN)_4Cu]PF_6$-modified GCE ($[(CH_3CN)_4Cu]PF_6$/GCE) were also prepared by the same procedure using Taniaphos or $[(CH_3CN)_4Cu]PF_6$ instead of the Taniaphos–Cu^+ complex.

Electrochemical characterization

Electrochemical characterization studies of different samples were carried out in a three-electrode cell consisting of the GCE modified with different samples as the working electrode, a platinum plate (10 × 5 mm) as the auxiliary electrode and an Ag/AgCl electrode (with saturated KCl solution) as the reference electrode. The electrolyte used was 0.1 M KCl containing 5 mM $[Fe(CN)_6]^{4-/3-}$. The CVs were recorded at a scan rate of 100 mV s^{-1}, and the EIS of different electrodes was conducted in the frequency range of 10^5 to 1.0 Hz at an open circuit potential of 0.23 V.

Electrochemical chiral discrimination of Trp, Tyr and Cys isomers

Unmodified GCE and GCE modified with $[(CH_3CN)_4Cu]PF_6$, Taniaphos and Taniaphos–Cu^+ complex were immersed in 20 mL of 0.1 M phosphate buffered saline (PBS, pH = 7.0) containing 1.0 mM L-Trp and D-Trp, respectively. After incubation at room temperature for 10 s, the DPVs of the Trp isomers combined with the modified electrodes were recorded, respectively, and the discrimination capability of different samples was evaluated based on the peak current ratio of D-Trp to L-Trp ($I_{D\text{-}Trp}/I_{L\text{-}Trp}$). The chiral discrimination of other electroactive AA (Tyr, Cys) isomers was determined by the same procedures by using Tyr or Cys instead of Trp. The construction of the chiral sensing platform and its application in the electrochemical chiral discrimination of the Trp isomers are depicted in Fig. 2.

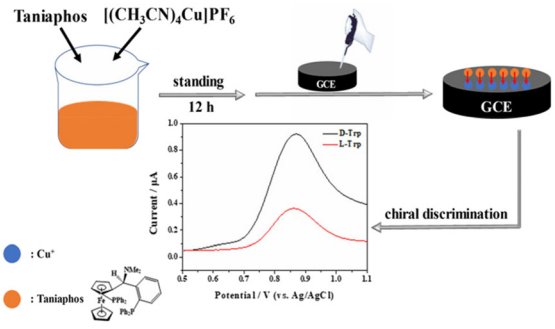

Fig. 2 Construction of the chiral sensing platform and its application in the electrochemical chiral discrimination of the Trp isomers.

This journal is © The Royal Society of Chemistry 2023

Published on 11 2023. Downloaded on 11.5.2026 19:23:17.

Results and discussion

SEM images of Taniaphos and the Taniaphos–Cu^+ complex

The SEM images of Taniaphos and the Taniaphos–Cu^+ complex are presented in Fig. 3. As can be seen, Taniaphos is composed of coral-shaped nanosheets with a porous structure (Fig. 3A), while the Taniaphos–Cu^+ complex displays a block-like structure (Fig. 3B). The quite different morphologies between Taniaphos and the Taniaphos–Cu^+ complex might be ascribed to the conversion of the agglomerated nanosheets of free Taniaphos ligand into microcrystals upon the complexation with Cu^+ from the $[(CH_3CN)_4Cu]PF_6$ metal precursor.[23]

FT-IR spectra of $[(CH_3CN)_4Cu]PF_6$, Taniaphos and the Taniaphos–Cu^+ complex

The FT-IR spectra of different samples are shown in Fig. 4. As can be seen, $[(CH_3CN)_4Cu]PF_6$ displays two strong peaks at 829 and 559 cm^{-1} (curve a), which are related to PF_6^-.[24,25] The peak located at 1651 cm^{-1} on the spectrum of Taniaphos (curve b) is due to the stretching of C=C from the cyclopentadienyl group ($C_5H_5^-$) of ferrocene,[26] which can also be observed on the spectrum of the Taniaphos–Cu^+ complex (curve c). In addition, a peak at 840 cm^{-1} related to the Cu–P bond[27] appears on the spectrum of the Taniaphos–Cu^+ complex, further confirming the successful synthesis of the Taniaphos–Cu^+ complex.

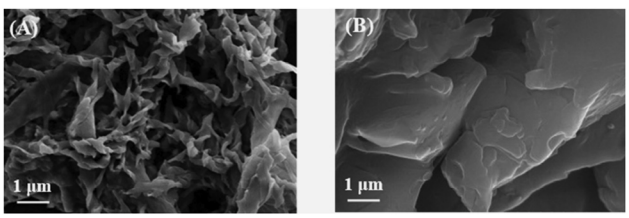

Fig. 3 SEM images of Taniaphos (A) and the Taniaphos–Cu^+ complex (B).

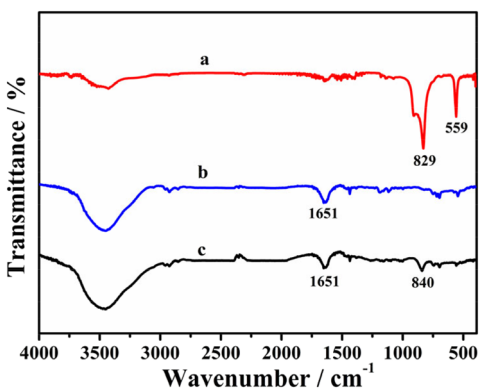

Fig. 4 FT-IR spectra of $[(CH_3CN)_4Cu]PF_6$ (a), Taniaphos (b) and the Taniaphos–Cu^+ complex (c).

XPS spectra of the Taniaphos–Cu^+ complex

The elemental composition and valence state of the Taniaphos–Cu^+ complex are investigated by XPS, and the results are presented in Fig. 5. Besides C, N, P and Fe, the element of Cu can be clearly observed at 923.9 eV on the XPS survey spectra (Fig. 5A), suggesting successful introduction of Cu^+ through the complexation with Taniaphos. Fig. 5B–F show the high-resolution XPS spectra of C 1s, N 1s, P 2p, Fe 2p and Cu 2p, respectively. The C 1s spectra display a single peak with a binding energy of 284.9 eV (Fig. 5B), which is characteristic of carbon in the $C_5H_5^-$ group ligated to the iron cation in ferrocene.[28] The N 1s spectra can be deconvoluted into two peaks at 399.7 and 402.0 eV (Fig. 5C), which are related to C≡N[29] originating from the metal precursor ($[(CH_3CN)_4Cu]PF_6$) and C–N[30] originating from Taniaphos, respectively. The P 2p spectra can be divided into three peaks at 130.9, 132.4 and 136.1 eV (Fig. 5D), corresponding to Cu–P,[31] C–P[32] and P–F,[33] respectively. In particular, the appearance of Cu–P indicates the complexation of Taniaphos with Cu^+ through coordination bonds. The two peaks at 708.0 and 720.9 eV on the Fe 2p spectra are assigned to Fe $2p_{3/2}$ and Fe $2p_{1/2}$, respectively (Fig. 5E), which are typical of ferrocene.[34,35] The two peaks located at 933.0 and 952.7 eV on the Cu 2p spectra can be ascribed to Cu $2p_{3/2}$ and Cu $2p_{1/2}$ corresponding to Cu–P (Fig. 5F),[36] further confirming the successful complexation of Taniaphos with Cu^+.

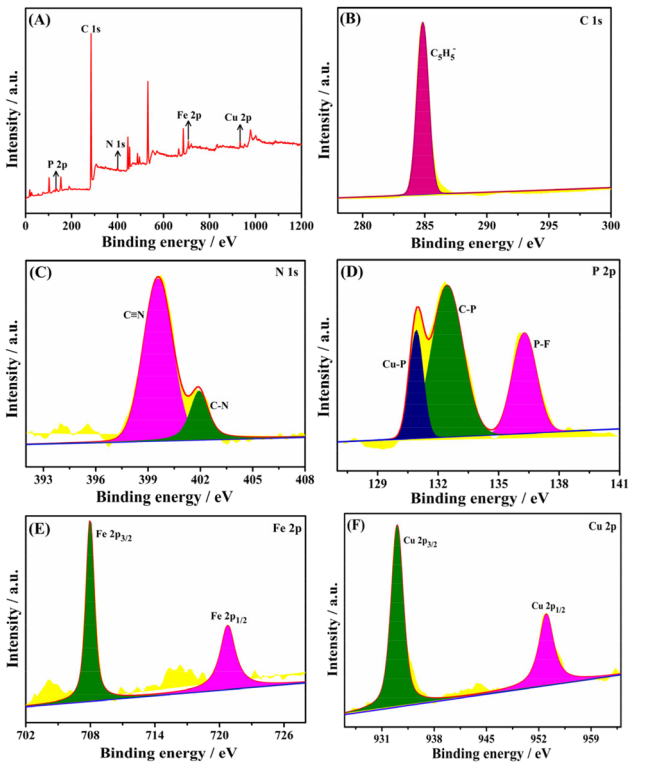

Fig. 5 XPS survey spectra (A) and high-resolution XPS spectra of C 1s (B), N 1s (C), P 2p (D), Fe 2p (E) and Cu 2p (F) of the Taniaphos–Cu^+ complex.

Published on 11 2023. Downloaded on 11.5.2026 19:23:17.

Electrochemical behavior of different electrodes

The CVs of different electrodes in 0.1 M KCl containing 5 mM $[Fe(CN)_6]^{4-/3-}$ are shown in Fig. 6A. There is a pair of well-defined redox peaks on the CV of the unmodified GCE (curve a), which is due to the conversion between $[Fe(CN)_6]^{4-}$ and $[Fe(CN)_6]^{3-}$. Compared with the unmodified GCE, the peak currents decrease significantly at the $[(CH_3CN)_4Cu]PF_6$/GCE owing to the poor conductivity of the metal precursor (curve b). The peak currents decrease further at the Taniaphos/GCE (curve c), which might be ascribed to the electrostatic repulsions between the two negatively charged $C_5H_5^-$ groups of Taniaphos and the $[Fe(CN)_6]^{4-/3-}$ probe. Note that the pair of redox peaks disappears almost completely at the Taniaphos–Cu^+/GCE (curve d), and the greatly inhibited electron transfer might be caused by the block-like structure of the Taniaphos–Cu^+ complex (Fig. 3B). Fig. 6B shows the Nyquist plots of different electrodes in the same electrolyte. There is a suppressed semicircle in the high frequency region for the four electrodes, corresponding to the charge transfer resistance (R_{ct}) at the electrode/solution interfaces.[37] As can be seen, the R_{ct} value of the Taniaphos–Cu^+/GCE (curve d) is remarkably larger than those of the unmodified GCE (curve a), $[(CH_3CN)_4Cu]PF_6$/GCE (curve b) and Taniaphos/GCE (curve c), agreeing well with the results of CV.

Electrochemical chiral discrimination of Trp isomers

Electrochemical chiral discrimination of the Trp isomers with different electrodes was investigated. The DPVs of different electrodes after incubation in 0.1 M PBS containing 1.0 mM L-Trp and D-Trp are presented in Fig. 7. As can be seen, the peak currents of the Trp isomers overlap almost completely at the unmodified GCE (Fig. 7A) and the $[(CH_3CN)_4Cu]PF_6$/GCE (Fig. 7B), suggesting poor discrimination capabilities of the two electrodes. The Trp isomers can be successfully discriminated at the Taniaphos/GCE since the value of $I_{D\text{-}Trp}/I_{L\text{-}Trp}$ can reach 1.56 (Fig. 7C). The higher peak currents of D-Trp at the Taniaphos/GCE might be attributed to the fact that both Taniaphos and the Trp isomers belong to aromatic systems (Taniaphos, benzene rings; Trp: indole ring), and Taniaphos preferably combines with D-Trp through π–π interactions,

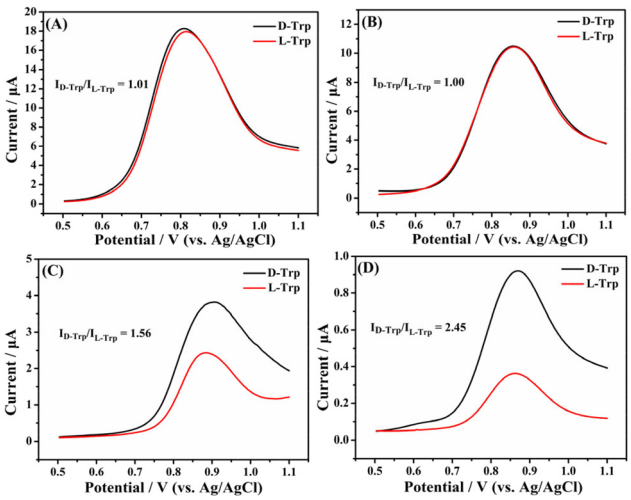

Fig. 7 Differential pulse voltammograms of an unmodified GCE (A), $[(CH_3CN)_4Cu]PF_6$/GCE (B), Taniaphos/GCE (C) and Taniaphos–Cu^+/GCE (D) after incubation in 0.1 M PBS containing 1.0 mM L-Trp and D-Trp.

which are prominent in aromatic systems[38] due to the opposite configurations of D-Trp and L-Trp (Fig. 8A). Excitingly, the discrimination capability is further enhanced at the Taniaphos–Cu^+/GCE ($I_{D\text{-}Trp}/I_{L\text{-}Trp}$ = 2.45, Fig. 7D), and the greatly enhanced discrimination capability might be ascribed to the shortened distance and easier π–π interactions between Taniaphos and D-Trp resulting from the formation of the Taniaphos–Cu^+-D-Trp ternary complex (Fig. 8B).

Wettability analysis of different samples

To further understand the preference of Taniaphos–Cu^+ for D-Trp, the water contact angles of stationary water droplets on different samples were measured and the results are presented in Fig. 9. Compared with the Taniaphos/GCE (63.4°, Fig. 9A), the water contact angle of the Taniaphos–Cu^+/GCE is remarkably increased to 91.4° (Fig. 9B), and the decreased hydrophilicity might be caused by the formation of the Taniaphos–Cu^+ complex. After incubation in 0.1 M PBS containing 1.0 mM L-Trp and D-Trp, the resultant ternary complexes (Taniaphos–

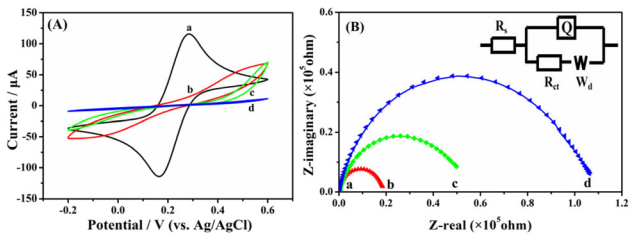

Fig. 6 Cyclic voltammograms (A) and Nyquist plots (B) of an unmodified GCE (a), $[(CH_3CN)_4Cu]PF_6$/GCE (b), Taniaphos/GCE (c) and Taniaphos–Cu^+/GCE (d) in 0.1 M KCl containing 5 mM $[Fe(CN)_6]^{4-/3-}$. Inset of (B): the equivalent circuit, where R_s, R_{ct}, W_d and Q represent the solution resistance, charge transfer resistance, Warburg resistance and constant phase elements, respectively.

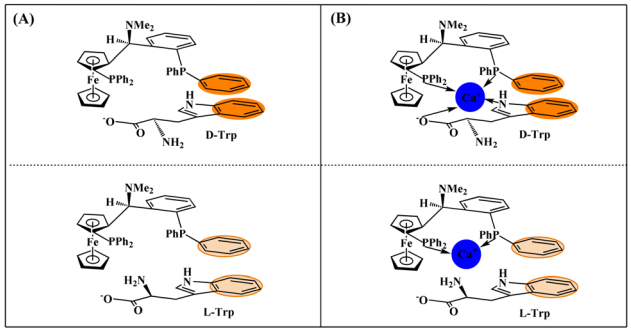

Fig. 8 Schematic illustrations showing the discrimination mechanisms of Taniaphos (A) and the Taniaphos–Cu^+ complex (B) toward the Trp isomers.

This journal is © The Royal Society of Chemistry 2023

Published on 11 2023. Downloaded on 11.5.2026 19:23:17.

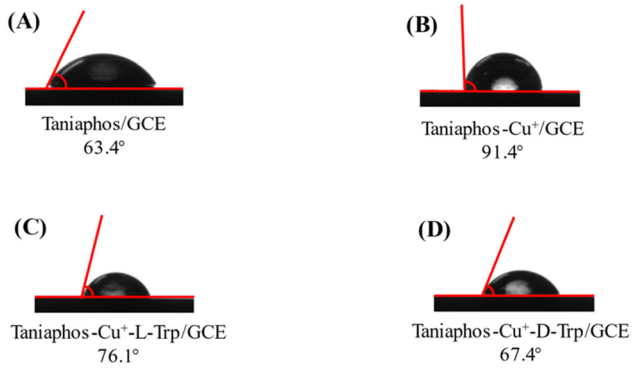

Fig. 9 Water contact angle values of the Taniaphos/GCE (A), Taniaphos–Cu^+/GCE (B), Taniaphos–Cu^+-L-Trp/GCE (C) and Taniaphos–Cu^+-D-Trp/GCE (D) with a representative picture.

Cu^+-D-Trp and Taniaphos–Cu^+-L-Trp) display smaller water contact angles than that of Taniaphos–Cu^+, which might be ascribed to the high hydrophilicity of the Trp isomers.[39] Note that the water contact angle of Taniaphos–Cu^+-L-Trp (76.1°, Fig. 9C) is larger than that of Taniaphos–Cu^+-D-Trp (67.4°, Fig. 9D), further confirming the preference of the Taniaphos–Cu^+ complex for D-Trp.

Optimization of the pH

The pH of the PBS for the incubation of the Taniaphos–Cu^+ complex is optimized. As shown in Fig. 10, the highest discrimination capability is achieved at pH 7.0. In acidic media (pH 5.0–6.5), Cu^+ in the Taniaphos–Cu^+ complex is easily disproportionated into Cu^{2+} and Cu, resulting in low stability of the complex and consequently decreased discrimination capability. In alkaline media (pH 7.5 and 8.0), the Trp isomers are negatively charged since their isoelectric point is ~5.89. Therefore, the electrostatic repulsions between the Trp isomers and the negatively charged $C_5H_5^-$ groups of Taniaphos will partially inhibit the combination of the Taniaphos–Cu^+ complex and the Trp isomers, leading to a remarkably decreased discrimination capability.

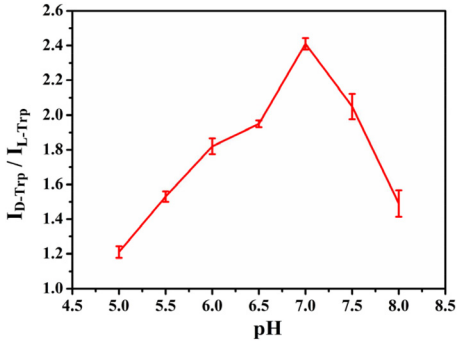

Fig. 10 Influence of pH on the discrimination capability of the chiral sensing platform.

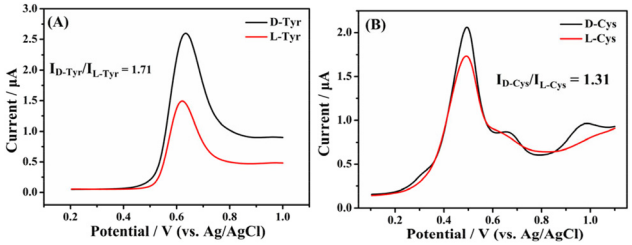

Fig. 11 Differential pulse voltammograms of the Taniaphos–Cu^+/GCE after incubation in 0.1 M PBS containing 1.0 mM L-/D-Tyr (A) and 1.0 mM L-/D-Cys (B).

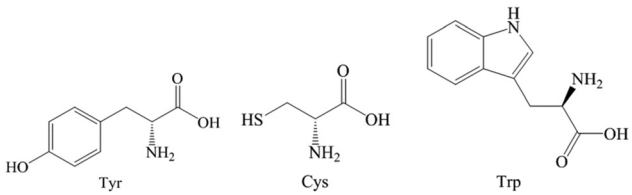

Fig. 12 Chemical structures of Tyr, Cys and Trp.

Electrochemical chiral discrimination of other electroactive AA isomers

Finally, the universality of the developed chiral sensing platform is investigated by discriminating the isomers of other electroactive AA including Tyr and Cys, and the results are presented in Fig. 11. As can be seen, the isomers of both Tyr (Fig. 11A) and Cys (Fig. 11B) can be successfully discriminated with the Taniaphos–Cu^+/GCE. However, the discrimination capability of the chiral sensing platform toward the isomers of Trp ($I_{D\text{-}Trp}/I_{L\text{-}Trp}$ = 2.45) is far higher than those toward the isomers of Tyr ($I_{D\text{-}Tyr}/I_{L\text{-}Tyr}$ = 1.71) and Cys ($I_{D\text{-}Cys}/I_{L\text{-}Cys}$ = 1.31). On the one hand, Trp and Tyr are aromatic AA while Cys is an aliphatic AA (Fig. 12), and thus the π–π interactions between Taniaphos and Cys are significantly weaker than those between Taniaphos and Trp and Tyr, leading to the lowest discrimination capability being toward the Cys isomers. On the other hand, Trp possesses an indole ring while Tyr possesses a benzene ring (Fig. 12), and therefore the π–π interactions between Taniaphos and Trp are stronger than those between Taniaphos and Tyr. As a result, the discrimination capability of the chiral sensing platform toward the Trp isomers is more pronounced than for the Tyr isomers (2.45 *vs.* 1.71).

Conclusions

A chiral sensing platform is constructed based on a Taniaphos–Cu^+ complex. Since the Taniaphos–Cu^+ complex can preferably combine with D-Trp to form the ternary complex of Taniaphos–Cu^+-D-Trp, Trp isomers can be successfully discriminated with the developed chiral sensing platform. Compared with the Taniaphos/GCE, the discrimination capability is further enhanced at the Taniaphos–Cu^+/GCE owing to

the shortened distance and easier π–π interactions between Taniaphos and D-Trp through the formation of the ternary complex. The preference of the chiral sensing platform for D-Trp can be further confirmed by the measurements of water contact angles of different samples. Besides, the Taniaphos–Cu^{+}/GCE can also be used for the chiral discrimination of other electroactive AA isomers including Tyr and Cys. Among the tested AA isomers, the highest discrimination capability is achieved for the Trp isomers due to the unique indole ring of Trp. The findings of this work indicate that the developed chiral sensing platform based on the multi-substituted ferrocene–Cu^{+} complex might have great potential for chiral analysis.

Conflicts of interest

There are no conflicts to declare.

Published on 11 2023. Downloaded on 11.5.2026 19:23:17.

Acknowledgements

This work was financially supported by the Science and Technology Program of Zhejiang Province (LGF22B050008), the Science and Technology Program of Jiaxing (2022AY10012), the Natural Science Foundation for Colleges and Universities in Jiangsu Province (20KJA150005, 21KJB150018, and 22KJB150018) and the Advanced Catalysis and Green Manufacturing Collaborative Innovation Center (ACGM2022-10-12). We also thank Mr Wenchang Wang from the Analysis and Testing Centre of Changzhou University for his assistance on SEM.

References

1 X. Q. Liang, Y. Z. Li, Z. Wang, S. S. Zhang, Y. C. Liu, Z. Z. Cao, L. Feng, Z. Y. Gao, Q. W. Xue, C. H. Tung and D. Sun, *Nat. Commun.*, 2021, **12**, 4966.
2 S. S. Wu, H. Wang, D. T. Wu, G. C. Fan, Y. X. Tao and Y. Kong, *Analyst*, 2021, **146**, 1612.
3 M. Jafari, J. Tashkhourian and G. Absalan, *Talanta*, 2018, **178**, 870.
4 X. H. Niu, X. Yang, Z. L. Mo, R. B. Guo, N. J. Liu, P. Zhao, Z. Y. Liu and M. X. Ouyang, *Electrochim. Acta*, 2019, **297**, 650.
5 Q. M. Ye, L. L. Guo, D. T. Wu, B. Z. Yang, Y. X. Tao, L. H. Deng and Y. Kong, *Anal. Chem.*, 2019, **91**, 11864.
6 D. M. Guo, Y. H. Huang, C. Chen, Y. Chen and Y. Z. Fu, *New J. Chem.*, 2014, **38**, 5880.
7 L. P. Bao, X. H. Chen, B. Z. Yang, Y. X. Tao and Y. Kong, *ACS Appl. Mater. Interfaces*, 2016, **8**, 21710.
8 J. Zou and J. G. Yu, *Mater. Sci. Eng., C*, 2020, **112**, 110910.
9 M. Wang, H. F. Cui, N. Hong, Q. X. Shu, X. R. Wang, Y. P. Hu, G. B. Wei, H. Fan and J. Zhang, *Sens. Actuators, B*, 2022, **358**, 131496.
10 T. J. Ning, F. S. Liao, H. F. Cui, Z. J. Yin, G. Q. Ma, L. Cheng, N. Hong, J. Xiong and H. Fan, *Microchim. Acta*, 2020, **187**, 340.
11 G. B. Zhu, O. J. Kingsford, Y. H. Yi and K. Y. Wong, *J. Electrochem. Soc.*, 2019, **166**, H205.
12 J. J. Xu, Q. H. Wang, C. Z. Xuan, Q. Xia, X. Lin and Y. Z. Fu, *Electroanalysis*, 2016, **28**, 868.
13 L. Gong, Q. Q. Zhao, S. S. Wu, Z. Z. Yin, D. T. Wu, W. R. Cai and Y. Kong, *Langmuir*, 2021, **37**, 14454.
14 Y. X. Tao, J. Y. Dai, Y. Kong and Y. Sha, *Anal. Chem.*, 2014, **86**, 2633.
15 J. Ou, Y. H. Zhu, Y. Kong and J. F. Ma, *Electrochem. Commun.*, 2015, **60**, 60.
16 P. J. Jing, Z. Z. Yin, W. R. Cai, J. Y. Li, D. T. Wu and Y. Kong, *Bioelectrochemistry*, 2022, **146**, 108110.
17 L. P. Bao, J. Y. Dai, L. Yang, J. F. Ma, Y. X. Tao, L. H. Deng and Y. Kong, *J. Electrochem. Soc.*, 2015, **162**, H486.
18 B. J. V. Verkuijl, A. J. Minnaard, J. G. de Vries and B. L. Feringa, *J. Org. Chem.*, 2009, **74**, 6526.
19 K. W. Tang, G. H. Wu, P. L. Zhang, C. S. Zhou and J. J. Liu, *Ind. Eng. Chem. Res.*, 2012, **51**, 15233.
20 A. Cayuelas, O. Larranaga, C. Najera, J. M. Sansano, A. de Cozar and F. P. Cossio, *Tetrahedron*, 2016, **72**, 6043.
21 Q. Zhang, X. S. Jia and L. Yin, *Tetrahedron*, 2019, **75**, 1676.
22 W. J. Xiao, S. H. Chen, X. Liu and Y. Ma, *Chirality*, 2021, **33**, 292.
23 A. Reiss, M. C. Chifiriuc, E. Amzoiu and N. Cioatera, *J. Therm. Anal. Calorim.*, 2018, **131**, 2073.
24 X. C. Li, X. L. Li, Z. Y. Zhang, L. Yang, B. H. Zhong and X. L. Wang, *J. Mol. Struct.*, 2015, **1094**, 9.
25 I. S. Kritchenkov, J. R. Shakirova and S. P. Tunik, *RSC Adv.*, 2019, **9**, 15531.
26 D. T. Wu, L. L. Tan, C. Ma, F. Pan, W. R. Cai, J. Y. Li and Y. Kong, *Anal. Chem.*, 2022, **94**, 6050.
27 V. V. Avdeeva, G. A. Buzanov, E. A. Malinina, N. T. Kuznetsov and A. V. Vologzhanina, *Crystals*, 2020, **10**, 389.
28 C. M. Woodbridge, D. L. Pugmire, R. C. Johnson, N. M. Boag and M. A. Langell, *J. Phys. Chem. B*, 2000, **104**, 3085.
29 S. Carniato, F. Rochet, J. J. Gallet, F. Bournel, G. Dufour, C. Mathieu and S. Rangan, *Surf. Sci.*, 2007, **601**, 5515.
30 X. Yang, X. H. Niu, Z. L. Mo, J. Wang, C. Shuai, Z. Pan, Z. Y. Liu, N. J. Liu and R. B. Guo, *J. Electrochem. Soc.*, 2019, **166**, B1053.
31 W. F. Liu, H. X. Gao, Z. Zhang, Y. F. Zheng, Y. H. Wu, X. T. Fu, J. Su and Y. H. Gao, *Chem. Eng. J.*, 2022, **437**, 135352.
32 D. W. Shin, T. S. Kim and J. B. Yoo, *Mater. Res. Bull.*, 2016, **82**, 71.
33 P. Brant, L. S. Benner and A. L. Balch, *Inorg. Chem.*, 1979, **18**, 3422.
34 S. C. Liu, J. Xu, E. G. Dai, J. J. Qiu and Y. Liu, *Microporous Mesoporous Mater.*, 2018, **264**, 133.
35 A. Rabti, C. C. Mayorga-Martinez, L. Baptista-Pires, N. Raouafi and A. Merkoci, *Anal. Chim. Acta*, 2016, **926**, 28.

This journal is © The Royal Society of Chemistry 2023

36 R. C. Shen, J. Xie, Y. N. Ding, S. Y. Liu, A. Adamski, X. B. Chen and X. Li, *ACS Sustainable Chem. Eng.*, 2019, **7**, 3243.
37 H. L. Ge, Y. Kong, Y. Pan, L. H. Deng, D. Shou and Q. Y. Lu, *J. Electrochem. Soc.*, 2015, **162**, G87.
38 R. Thakuria, N. K. Nath and B. K. Saha, *Cryst. Growth Des.*, 2019, **19**, 523.
39 S. S. Wu, Z. Z. Yin, D. T. Wu, Y. X. Tao and Y. Kong, *Langmuir*, 2019, **35**, 16761.

Published on 11 2023. Downloaded on 11.5.2026 19:23:17.